A computational investigation of laminar shock/wave boundary layer interactions

N. R. Deepak, S. L. Gai and A. J. Neely
deepak.narayan@gmail.com
School of Engineering and Information Technology
The University of New South Wales, Australian Defence Force Academy
Canberra, Australia

ABSTRACT

Hypersonic laminar flow past a compression corner has been numerically investigated using time-accurate computational fluid dynamics (CFD) approach. Two flow conditions were considered relevant to high and low enthalpy conditions with a total specific enthalpy of 19MJ/kg and 2·8MJ/kg. The Mach number and unit Reynolds number per metre were 7·5, 9·1 and $3{\cdot}10 \times 10^5$ and $32{\cdot}2 \times 10^5$ respectively. These free stream conditions provided attached, incipiently separated and fully separated flows for ramp angles between $\theta_w = 5°$ to 24°. A grid independence study has been carried out to estimate the sensitivity of heat flux and skin friction in the strong interaction regions of the flow. The investigation was carried out assuming the flow to be laminar throughout and high temperature effects such as thermal and chemical nonequilibrium are studied using Park's two temperature model with finite rate chemistry. A critical comparison has been made with existing steady state computational and experimental data and the study has highlighted the importance of high temperature effects on the flow separation and reattachment.

Paper No. 3802. Manuscript received 13 December 2011, revised version received 29 February 2012, accepted 9 March 2012.

https://doi.org/10.1017/S0001924000007740 Published online by Cambridge University Press

NOMENCLATURE

c_f	local skin-friction co-efficient
Cp	coefficient of heat capacity (constant pressure) [J/kgK]
Cv	coefficient of heat capacity (constant volume) [J/kgK]
h_r	recovery enthalpy [MJ/kg]
h_w	wall enthalpy [MJ/kg]
H	enthalpy [MJ/kg]
k	coefficient of thermal conductivity [W/mK]
L_c	forebody flat plate length
M	Mach number
p	pressure [Pa]
Pr	Prandtl number
q_w	heat flux [W/m^2]
R	reattachment
Re	Reynolds number
Re/m	unit Reynolds number [1/m]
s	wetted surface
S	separation
St	Stanton number
t	time [s]
T	temperature [K]
T_t	translational temperature [K]
T_v	vibrational temperature [K]
u	x-component of velocity [ms^{-1}]
U	algebraic vector of conserved quantities
X_i	species mass fraction

Greek symbols

γ	ratio of specific heats
Δt	time scale or time step [s]
Δw	first cell spacing from wall
Δx	grid spacing in x-co-ordinate [m]
Δy	first cell spacing from wall
θ_w	wedge angle [degree]
μ	coefficient of viscosity [kg/m^{2}s]
ρ	density [kg/m^3]
τ_w	shear stress [Pa]

Subscripts and superscripts

c	compression corner
e	edge conditions
o	total conditions
w	wall conditions
∞	freestream conditions

https://doi.org/10.1017/S0001924000007740 Published online by Cambridge University Press

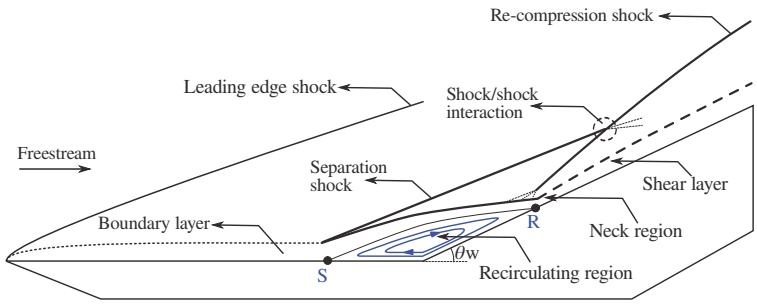


Figure 1. Schematic representation of flow features over a compression corner.

Acronyms and abbreviations

AUSMDV	advection upwind splitting method combining difference and vector splitting
CEA	chemical equilibrium with applications
CFL	Courant-Friedrichs-Lewy
CFD	computational fluid dynamics
GCI	grid convergence index
MUSCL	monotone upstream-centered schemes for conservation laws
NO	molecular nitric oxide
O_2	molecular oxygen
O	atomic oxygen
QSS	quasi steady state

1.0 INTRODUCTION

Hypersonic flow past a compression corner is a typical problem of shock wave/boundary layer interaction (SWBLI). The importance of SWBLI on aerothermodynamic characteristics has led to its extensive investigation due to its relevance in the design of hypersonic space vehicles. While the compression corner problem appears to be a simplified geometric configuration, it is analogous to a number of generic regions of separated flow on a space vehicle. In high enthalpy hypersonic flow, the total energy content is sufficiently high to cause changes in the internal distribution of energy levels within the gas. This leads to molecular excitation that eventually induces chemical reactions via dissociation and ionisation. Understanding SWBLI under such a scenario is therefore necessary for the reliable design of space vehicles.

The features of hypersonic laminar flow past a two-dimensional compression corner are illustrated through a schematic representation in Fig. 1. It is characterised by a boundary layer over the flat plate with a leading edge shock. The existence of the corner causes a shock wave (ramp shock) that results in a gradual pressure rise due to the interaction with the boundary layer. For sufficiently large corner angle (θ_w), the shock wave is strong enough to cause boundary layer separation (*S*) upstream of the corner forming a separation bubble with recirculating flow. A separation shock wave in turn forms at the location where the boundary layer separates. Downstream from the corner the separated shear layer reattaches (*R*) to the surface. When reattachment occurs, the thickness of the shear layer is reduced as the flow accelerates and turns towards the surface forming a *neck*. The compression waves thus generated coalesce to form a

https://doi.org/10.1017/S0001924000007740 Published online by Cambridge University Press

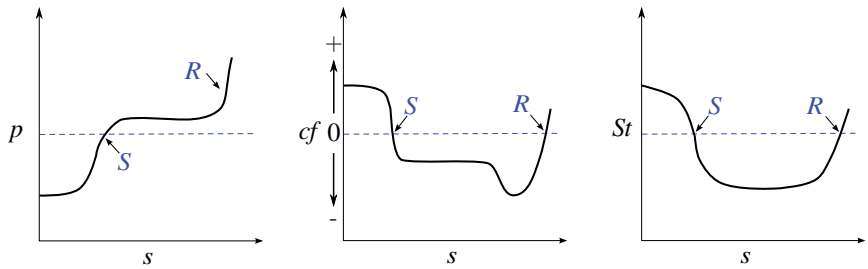


Figure 2. Schematic distribution of surface parameters over a compression corner.

reattachment shock. Downstream of reattachment the shear layer grows and the flow eventually becomes parallel to the surface. Depending upon the freestream Mach number, the leading edge shock may interact with the separation or reattachment shock. Similarly, the separated shock may interact with the reattachment shock forming a shock/shock interaction with the emergence of a slip stream.

Typically, the distributions of heat flux, skin friction and pressure upstream of the corner are similar to those over a flat plate. Due to adverse pressure gradient, caused by the presence of the corner, the pressure increases, but both heat flux and skin friction decrease. For a fully separated flow, the skin friction changes to negative and becomes positive after reattachment. The heat flux has a typically rounded distribution. The pressure distribution shows a plateau after an initial rise and shows a rapid rise at reattachment. Figure 2 shows typical distributions of pressure, skin friction and heat flux.

The compression corner is a convenient configuration to examine the SWBLI and therefore has been widely studied both numerically as well as experimentally ranging from supersonic to hypersonic flows. Some of the early work include those by MacCormack[1] and Hung[2,3] using full two-dimensional Navier-Stokes solutions with time-accurate approach. Subsequently, MacCormack[4] devised a new approach combining explicit and implicit methods to investigate two-dimensional SWBLI. Similar strategy was also adopted by Madhavan and Swaminathan[5] to solve supersonic compression corner flows. Experimental data by Holden and Moselle[6] have been subjected to numerous computational studies using different techniques. Probably, one of the first simulation exercise to be carried out appears to be by Hung[2,3] using time-accurate Navier-Stokes calculations. Fay and Sambamurthi[7], simulated, using finite-volume approach and further compared their numerical data with those of Rudy *et al*[8], who carried out both two and three-dimensional simulations for the same data of Holden and Moselle[6]. Lee and Lewis[9] further examined the same configuration, while Gaitonde and Shang[10] investigated the influence of different numerical methods. Simeonides and Haase[11] in addition to laminar flow considered transitional and fully turbulent studies using time-accurate approach. All studies, however, have been carried out under low enthalpy conditions or predominantly under perfect gas assumption.

Grumet *et al*[12] were perhaps first to investigate the high temperature chemical nonequilibrium effects in SWBLI for two-dimensional flows using finite-rate chemistry. This was further extended by Wu *et al*[13] to include the effects of radiation. Following these works, Grasso and Leone[14] and Furumoto *et al*[15] studied nonequilibrium effects at enthalpies up to 18MJ/kg for air. Olejniczak and Candler[16] performed detailed computational investigation for the experiments of Mallinson *et al*[17] assuming thermo-chemical nonequilibrium for enthalpy ranging from 2·8 to 19MJ/kg. More recently, Davis and Sturtevant[18] and Matsumoto *et al*[19]

https://doi.org/10.1017/S0001924000007740 Published online by Cambridge University Press

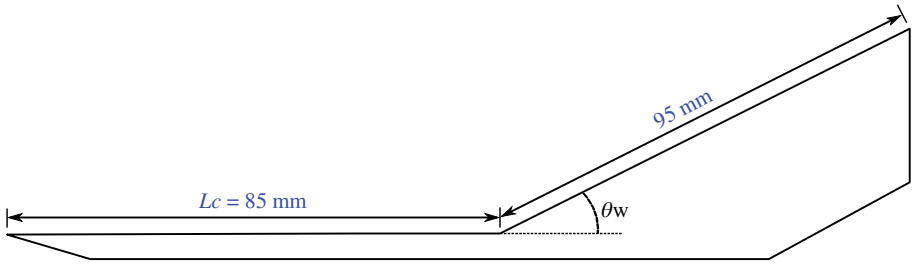


Figure 3. Compression corner geometry.

studied SWBLI at high enthalpy flows including finite rate chemistry. Despite these computational efforts in studying high temperature effects in SWBLI, there is still a need for comprehensive comparison between experiments and computations. At high enthalpy conditions, high temperature effects are inherently present and thus the significance of these in regions of SWBLI is an important aspect. This necessitates a thorough validation of computational codes and physico-chemical model used to compare with the experimental data.

The current study therefore aims to compliment the high enthalpy experiments carried out by Mallinson[17,20] with numerical investigation. Mallinson[17,20] carried out a comprehensive investigation of the SWBLI at a compression corner in a free-piston driven shock tunnel facility. Complete descriptions of the operation of this facility can be found in Refs 21-23. The total specific enthalpy considered in these experiments were 2·8MJ/kg and 19MJ/kg with air as the test gas. The freestream Mach and the Reynolds number provided attached, incipiently separated and fully separated flow conditions for ramp angles between $\theta_w = 5°$ to $\theta_w = 24°$. Previous studies at similar ramp angles by Holden and Moselle[6] were restricted to quite low enthalpy conditions, where high temperature effects were mostly insignificant. Mallinson[20] conducted his experiments at higher enthalpies to investigate the high temperature effects, if any. His conclusion was that high temperature effects were not significant. The present paper re-examines this aspect and provides critical comparison between computations and his experimental data.

2.0 GEOMETRY AND FLOW CONDITIONS

The geometry consists of an upstream forebody flat plate (L_c) of 85mm with a sharp leading edge followed by a ramp of 95mm. This configuration is studied at three ramp angles (θ_w) of 24°, 18° and 16° for high enthalpy flow of 19MJ/kg designated as condition B[17,20] and they represent fully separated, incipiently separated and attached flows respectively. For the low enthalpy condition G (2·86MJ/kg) only 18° and 10° representing fully separated and incipiently separated flows are considered. Schematically, the configuration is presented in Fig. 3.

The co-ordinate system used for the compression corner is achieved by normalising the wetted surface (s) with the upstream plate length (L_c), such that the corner location has a value of $s/L_c = 1·0$. This type of normalisation was used by Mallinson[20] to present experimental results over the compression corner and, the same system is used to present the computational results. The computations are performed utilising the flow properties as evaluated by Mallinson[17,20]. Table 1 details the flow parameters, along with species concentrations, as reproduced in Mallinson[20] for the computational simulations. For the thermal non-equilibrium computations, the vibrational temperature (T_v) is assumed to be in equilibrium with the translational temperature (T_t).

https://doi.org/10.1017/S0001924000007740 Published online by Cambridge University Press

Table 1
T3 flow conditions

Flow parameter	Condition B	Condition G
Test gas	Air	Air
H_0 [MJ/kg]	19·0	2·83
p_∞[kPa]	0·99	0·73
T_∞[K]	1,160	160
ρ_∞[kg/m^3]	$2{\cdot}60 \times 10^{-3}$	$16{\cdot}0 \times 10^{-3}$
u_∞[ms^{-1}]	5,470	2,280
M_∞	7·5	9·1
γ_∞	1·45	1·40
Re_∞[1/m]	$3{\cdot}10 \times 10^5$	$32{\cdot}2 \times 10^5$
X_{N_2}	0·750	0·78
X_N	0·001	–
X_{O_2}	0·060	0·22
X_O	0·159	–
X_{NO}	0·030	–

The computations presented here were carried out under the assumption of two-dimensional flow. Experimental investigation by Mallinson[20] has shown that the hypervelocity flow over a compression corner can be at least nominally two-dimensional over the mid-span. This was established through examining heat transfer and pressure traces at different on and off-centre locations upstream of the corner within the separated region for a fully separated flow. The models were experimented with and without side fences attached and it was shown that the traces were nearly identical in both cases at the same axial and span wise locations, which confirms the flow to be reasonably two-dimensional for a fully separated flow.

3.0 COMPUTATIONAL APPROACH

3.1 Computational code and models

The two-dimensional flow field over the compression corner was modelled using compressible Navier-Stokes solver, Eilmer-3[24,25]. One of the primary reasons for using Eilmer-3 in this investigation is its capability to study the thermo-chemical nonequilibrium behaviour of air utilising two-temperature kinetic model of Park[26]. This feature has only recently been implemented in Eilmer-3 and is explored in this study. A brief description of the modelling approach used by Elimer-3 is presented here but a more comprehensive account is given in Ref. 27. Eilmer-3 solves time-accurate Navier-Stokes equations in two and three dimensions using a cell-centred finite-volume approach. The integral form of Navier-Stokes equations are used to represent the discretised cells, in which the cell-averaged quantities are updated using flux-based calculators.

https://doi.org/10.1017/S0001924000007740 Published online by Cambridge University Press

The code uses the van Albada[28] limiter and the Monotone Upstream-centred Schemes for Conservation Laws (MUSCL)[29,30] reconstruction scheme to obtain a second order upwind interpolation. While the inviscid fluxes are calculated at the cell interfaces using advection upwind splitting method combining difference and vector splitting (AUSMDV)[31], the viscous fluxes are calculated using the averaged values of the viscous stresses at the cell vertices. The time integral is numerically iterated using the predictor-corrector scheme and the time advancement is based on the time-splitting or operator-splitting technique[25,32]. Explicit time integration is used and numerical stability is maintained via the Courant-Friedrich-Lewy (CFL) criterion and the stability is achieved in the range $0 \leq \mathrm{CFL} \leq 0{\cdot}5$. Hence, all the CFD computations are performed with a CFL value of 0·5.

The simulations were performed under the assumption of both perfect gas and chemical plus thermal nonequilibrium effects. For the CFD calculations involving a perfect gas assumption, the test gas is assumed to behave as a single species while the thermodynamic behaviour was calorically perfect with a constant ratio of specific heats (γ). Viscosity was modelled using Sutherland formulation and thermal conductivity was calculated using $k = \mu Cp/Pr$ assuming a Prandtl number of 0·72. For simulations involving chemical plus thermal nonequilibrium, the test gas was modelled as five species and mass fractions relevant to the conditions given in Table 1 are used. Chemical plus thermal nonequilibrium simulations were performed using Park[26] scheme described by 23 reactions for high temperature air represented by 11 species aimed at modelling dissociation-recombination and exchange and ionisation reactions. In the current investigation, only five neutral species (N_2, O_2, NO, O and N) that contribute towards dissociation-recombination and exchange reactions are considered and the effects of ionisation are ignored. This is because with the nonequilibrium flow over a slender body, the dissociated species may not be subjected to ionisation, unlike the forebody region of a blunt body. Therefore, modelling with five neutral species should be a reasonable assumption. This scheme has received particular attention in recent years, due to its capability of modelling two temperatures at an additional cost of solving only a single partial differential equation for the total vibrational energy[33]. As this model is computationally less expensive than a more complicated multi-temperature model, it is widely implemented in CFD codes[33].

For the set of chemical kinetic schemes, the reaction rate coefficients were calculated based on the generalised Arrhenius form. The finite-rate chemical reactions were modelled as a set of ordinary differential equations using a quasi-steady state method, alpha-QSS[34]. Another important criterion to be considered here is to ensure that the mass due to a chemical reaction is conserved at every chemical time step. This is achieved by scaling the mass fraction of the participating species at the end of every time step such that the mass due to chemistry is conserved[32]. This approach is called renormalisation and is believed to be more accurate than the common approach of solving $(N - 1)$ species for conservation[32]. The thermodynamic behaviour for these reactive species is based on the mixture of thermally perfect gases. Therefore, the species have perfect collisional behaviour and the values of Cp and Cv are functions only of the temperature. The values of Cp are modelled individually for every species using a polynomial curve fit outlined by NASA Glenn computer code program, CEA (Chemical Equilibrium with Applications)[35,36] which is valid up to 20,000K. The modelling of transport properties is again based on the CEA approach in which the individual species properties are first modelled from the CEA polynomial curve fits and then the Gupta[37] mixing rule is used to compute viscosity and thermal conductivity of the mixture. Diffusion among the various species due to the concentration gradient occurring via chemical reactions is modelled using Fick's law.

https://doi.org/10.1017/S0001924000007740 Published online by Cambridge University Press

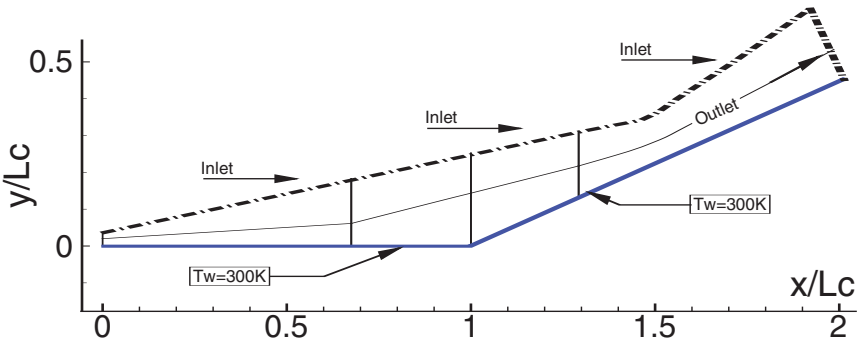


Figure 4. Computational domain and boundary conditions for $\theta_w = 24^\circ$ compression corner model.

3.2 Grid independence study

The grid independence study is performed for a ramp angle of $\theta_w = 24^\circ$ for condition B, which has the highest specific total enthalpy of 19MJ/kg. As indicated previously, because this configuration produces a fully separated flow with a strong inviscid/viscous interaction, a grid independence obtained under this condition should be sufficient for 18° and 16°, including for condition G, which is low enthalpy flow of 2·86MJ/kg.

Figure 4 shows the computational domain, which is divided into multiple blocks. The multi-block grid consists of 16 blocks which are precisely interconnected node-to-node. Although not indicated in the figure, the far upstream block has a free-slip wall. This ensures that the boundary layer growth from the sharp leading edge is not affected and the inflow condition is well posed. For the purpose of computational modelling a zero bluntness leading edge is assumed. The inflow topology of the grid shown in Fig. 4 is designed such that the leading edge shock is fully contained and aligned to it. For the region, where reattachment is know to occur, the topology is modified such that more refinement occurs naturally following the neck region and reattachment shock. In general, the topology is manually tailored to capture some of the flow physics, such as the separation region, separation shock and reattachment shock.

The flat plate and ramp walls are modelled as cold walls with a fixed temperature of T_w = 300K. This should be a valid assumption as during experiments, the rise in surface temperature is quite small even at high enthalpy conditions due to the short test times. Other investigators[38,39] have also modelled the wall temperature under similar assumptions. The top external boundaries are used to provide uniform supersonic inlets and the supersonic outlet is provided at the trailing edge of the downstream ramp. The grid independence study employs the freestream conditions presented in Table 1 and is performed using the assumption of perfect gas[8,11,40-43]. This can be justified on the following grounds. Firstly, in the perfect gas assumption, air is modelled as a single species, while for the reacting gas, air is generally treated as a multiple species; the only difference then is that the latter takes longer for convergence. For the current grid converged solution, the smallest grid size (Δy) is 20μm so that the time step (Δt) will be of the order of 1×10^{-9}s, based on a freestream velocity of 5,470ms^{-1} with a CFL value of 0·5. To attain a steady state solution, it takes approximately 280μs for the high enthalpy flow. The total time steps required are $\sim 1 \times 10^6$. Therefore, even for a perfect gas analysis the computational time requirements for solving these many time steps would be prohibitively expensive.

https://doi.org/10.1017/S0001924000007740 Published online by Cambridge University Press

Table 2
Various grids used for grid independent study

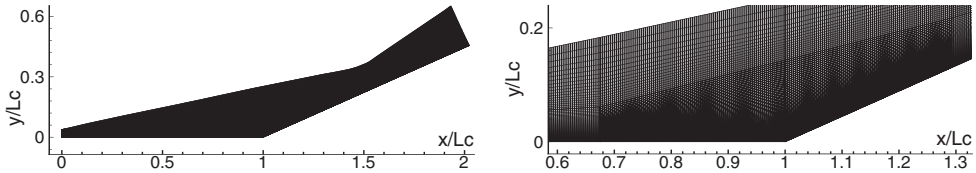
Grid	$i \times j$	Δ_w
Grid-1	100 × 20	100μm
Grid-2	215 × 40	50μm
Grid-3	340 × 60	25μm
Grid-4	480 × 84	20μm
Grid-5	570 × 102	20μm
Grid-6	684 × 102	20μm

This has also been noted by Druguet *et al*[44]. Other researchers, such as Gollan[42], Druguet *et al*[43] and Park *et al*[45] have also adopted the strategy of using perfect gas for grid independence studies. Consequently, the present grid independence study is limited to perfect-gas assumption. It is, therefore, possible that while the effects associated with high temperature effects may cause some small quantitative shifts, they are likely not to result in any major qualitative change. As a time-accurate code is being used, certain assumptions have been made. Firstly, an exact starting scenario of shock tunnel is not simulated here as this is beyond the scope of the present work. Nevertheless, the initial conditions such as pressure, velocity and temperature are applied similar to the conditions that are present in the test section at t = 0s. These conditions are, of course, uniform and are initialised from every grid point in the computational domain, including at the solid boundaries. Secondly, the inflow boundary conditions are tailored to accommodate uniform freestream properties along the oblique inlets of the computational domain (see Fig. 4). This does not account for any spatial flow non-uniformity that may be present in the actual start-up process.

Jackson *et al*[46] and others[47,48] consider the surface heat flux to be one of the critical variables for determining grid independence, as this is said to provide a sensitive test for computational calculations. In the present investigation, therefore, surface heat flux is considered for determining grid independence. In addition, we also consider the skin friction coefficient. The initial grid (Grid-1) has a distribution of $100i \times 20j$ with Δ_w = 100μm. Initialisation of the CFD simulation is performed with zero velocity and a pressure of 50Pa. The flow is simulated in a time-accurate manner, until the flow variables converge to steady conditions. Normalised heat fluxes (Stanton numbers) are computed on the flat plate and ramp surfaces. A subsequent refinement of the grid is carried out with the cells in both the i and j directions doubled and Δ_w reduced by a factor of 0·5. Details of the grid configuration are in Table 2. The growth rate of the grids in the boundary layer is based on the hyperbolic expansion law[49] with an expansion factor of 1·03. With this function, sufficient cells are placed close to the wall in order to capture the solution with good accuracy. For the leading edge, the grid clustering is carried out such that the first cell height is at $\Delta_x = \Delta_y = \Delta_w$ and a bi-geometric expansion is used in the streamwise direction with a ratio of 1·1. This type of refinement is critical for the prediction of the boundary layer over the flat plate. All the grids used here are therefore varied systematically to account for the leading edge grid resolution. The grid distribution for Grid-5 is shown in Fig. 5 in which, it can be seen that any variations in the grid are uniform.

The Stanton number distributions over the compression corner are shown in Fig. 6 for Grid-1 to Grid-5 showing the sensitivity in the vicinity of separation and reattachment (Fig. 6(b)). The Stanton number distributions are estimated from Equation 1, where, q_w is the surface heat flux estimated with first order approximation as $q_w = k(\partial T/\partial y)$, and h_r is the recovery enthalpy

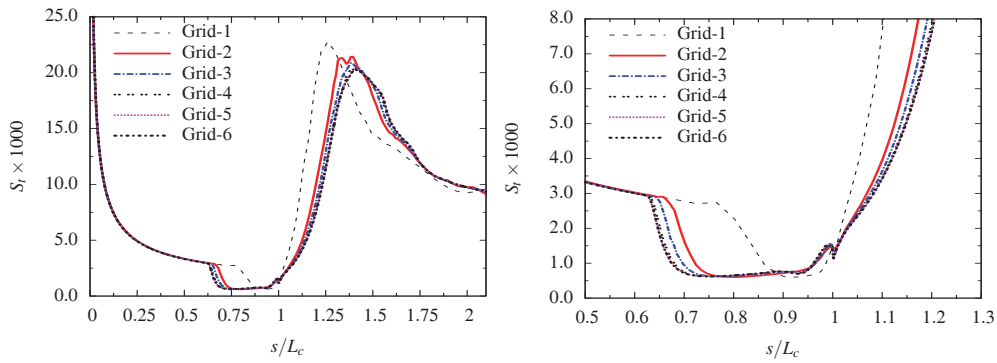
https://doi.org/10.1017/S0001924000007740 Published online by Cambridge University Press



(a) Representation of the grid in the computational domain

(b) Details of the grid in vicinity of corner

Figure 5. Distribution of grids for $\theta_w = 24^\circ$ compression corner.



(a) Stanton number distribution over entire wetted surface

(b) Stanton number distributions in vicinity of corner, $0{\cdot}5 \le s/L_c \le 1{\cdot}3$

Figure 6. Stanton number sensitivity over compression corner for condition B, H_0 = 19MJ/kg, $\theta_w = 24^\circ$.

evaluated as in Equation (2).

$$S_t = \frac{q_w}{\rho_e u_e (h_r - h_w)} \qquad \ldots (1)$$

$$h_r = h_e + \sqrt{P_r}\,\frac{u_e^2}{2}. \qquad \ldots (2)$$

It is seen from Fig. 6 that, in the region $0 \le s/L_c \le 0{\cdot}625$ there is not a great deal of variation in the heat flux but that, in the region $0{\cdot}625 \le s/L_c \le 0{\cdot}75$, significant changes are manifest. Grid-1 severely under estimates the separation location and with further grid refinement, the separation size appears to increase. This trend has also been noted by Simeonides and Haase[11], Olejniczak and Candler[16], Candler *et al*[50]; and Gnoffo[42]. This happens because, separation in this configuration is known to be extremely sensitive to grid refinement. Only after Grid-5, is there no change in the value of the Stanton number at separation (Fig. 6(b)). Soon after separation, within the recirculation region, no great changes are seen except for Grid-1. This suggests that, although the heat flux may be insensitive within the recirculation region with a sufficiently refined grid, adequate grid resolution is required to predict the proper scale of separation and its location. It is also noted that the heat flux is relatively insensitive to grid size upstream of separation, an observation also made by Simeonides and Haase[11].

https://doi.org/10.1017/S0001924000007740 Published online by Cambridge University Press

Downstream of the reattachment, $s/L_c \approx 1{\cdot}2$ (Fig. 6(a)), significant variations are seen close to the peak heat flux location. While, Grid-1 can be seen to over estimate the heat flux until it reaches a peak value, further downstream it under estimates it in comparison with the other grids. With more refinement, the heat flux prior to the peak as well as the peak itself shows a decrease. This is consistent with what was observed by Olejniczak and Candler[16]; and Candler *et al*[50] and is an indication that both reattachment and peak heat flux locations are very sensitive to grid size. Beyond $s/L_c \approx 1{\cdot}75$, in the region where the heat flux gradually reduces, again not much grid sensitivity is seen. Overall, beyond Grid-5, the heat flux becomes insensitive to grid size throughout the interaction region, upstream of separation and downstream of reattachment. It should be pointed out here that the increase in grid refinement from Grid-5 to Grid-6 is only in the stream wise direction (see Table 2). Further discussion on this point is presented in the following paragraphs.

The value of Δ_w has a significant effect on Stanton number predictions. Between Grid-1 and Grid-3, the value of Δ_w is reduced by a factor of 0·5 starting from 100μm (Table 2). This has a significant effect on the heat flux at the peak location, but seems not to be very sensitive upstream of the location of separation. From Grid-4 to Grid-5, Δ_w is further reduced. Although similar changes in Stanton number are seen, they are not as significant as those between Grid-1 to Grid-3. Between Grid-5 and Grid-6, there is no change in the value of Δ_w but only a change in the grid size in *i* (streamwise) direction, while the grid size in *j* (normal) direction remains the same. No change in the Stanton number is seen which reinforces the observation that the Stanton number is sensitive to Δ_w and not just the grid distribution. It was further noted that any increase in grid size in *j* direction beyond 102 grids without concurrently increasing the domain size in *j* direction, with $\Delta_w = 20\mu m$, would lead to grid distortion. This is a consequence of the grid algorithm that is used. Not only would this have an undesirable effect, but it also reduces the time-step value further leading to excessive computational time. Therefore, all further calculations have been made with $\Delta_w = 20\mu m$.

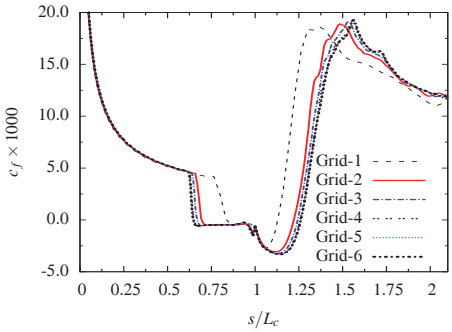
When comparing the current grid resolved solution with those of Olejniczak and Candler[16], certain points need to be noted. In their grid convergence study significant differences in the solution were noted when grids were increased from 512 × 512 to 1,024 × 1,024 for $\theta_w = 24°$. In particular, the finest grid shows the lowest heat flux distribution downstream of reattachment and a lower peak than experiments. However, Olejniczak and Candler[16] do not explicitly discuss about the influence of first cell height, which also has an effect on heat flux and skin friction as presently shown. Recently, Marini[51] used explicit Navier-Stokes approach to numerically investigate hypersonic flows over compression corners ranging from $\theta_w = 15° - 30°$. Here, it is shown, for $\theta_w = 24°$, that a grid resolution of 164 × 64 is able to reasonably match the experimental heat flux and pressure data of Holden and Moselle[6], both upstream and downstream from the corner. Nevertheless, Marini notes that a true grid independence was achieved only in the case of $\theta_w = 15°$ under the assumption of two-dimensionality.

Figure 7 presents skin friction coefficient sensitivity over the compression corner and in the separation/reattachment regions which shows that it follows those of the Stanton number. In Fig. 7(b), variations in the region of separation and reattachment are shown with respect to different grids. The skin friction coefficients presented in Fig. 7 are evaluated using Equation (3).

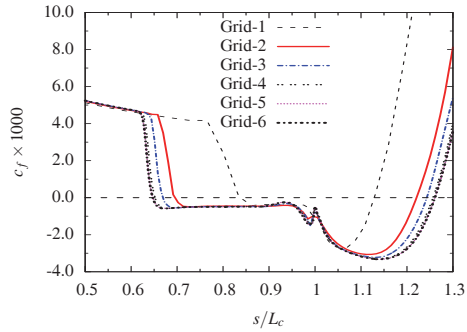
$$c_f = \frac{2\tau_w}{\rho_\infty u_\infty^2} \qquad \ldots (3)$$

where ρ_∞ and u_∞ are freestream density and velocity respectively. τ_w is the shear stress at the wall, $y = 0$, given by $\tau_w = \mu(\partial u/\partial y)$

https://doi.org/10.1017/S0001924000007740 Published online by Cambridge University Press



(a) Skin friction coefficient distribution over entire wetted surface



(b) Skin friction coefficient in vicinity of corner, $0{\cdot}5 \leq s/L_c \leq 1{\cdot}3$

Figure 7. Skin friction coefficient sensitivity over compression corner for condition B, H_0 = 19MJ/kg, $\theta_w = 24°$.

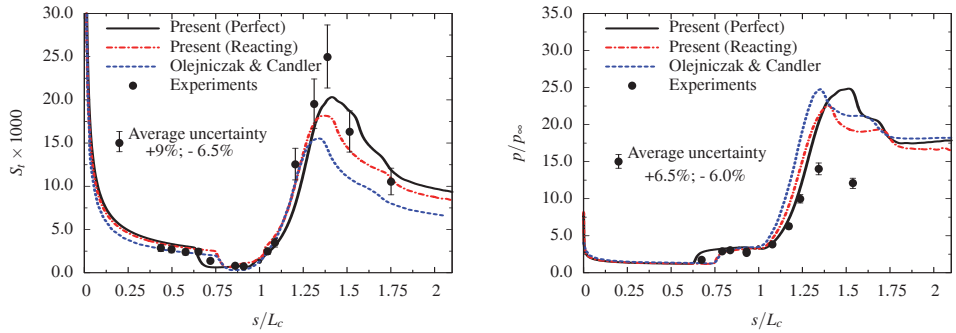
Table 3
Separation and reattachment distances for different grids at $\theta_w = 24°$

Grid	Separation (s/L_c)	GCI_s	Reattachment (s/L_c)	GCI_s
Grid-1	0·848	2·84E-01	1·112	1·49E-01
Grid-2	0·696	4·40E-02	1·224	4·67E-02
Grid-3	0·668	2·99E-02	1·243	1·26E-02
Grid-4	0.652	1·92E-02	1·256	1·61E-02
Grid-5	0·645	2·03E-02	1·260	1·43E-02
Grid-6	0·646	2·90E-03	1·260	4·26E-04

While the changes with grid size are very similar to those of heat flux, there are some notable differences downstream of the corner. Here, the peak skin friction coefficient in the negative scale increases as the grid is refined. Such a behaviour is also apparent in the data of Simeonides and Haase[11] and Candler *et al*[50]. This possibly occurs because, with refined grids and reduced Δ_w, the velocity gradients are properly captured within the recirculating flow. Subsequently, over the ramp surface after reattachment, the peak location changes with respect to the grid, although the magnitude does not seem to vary greatly between the grids.

The non-dimensional separation and reattachment locations for different grids taken from Fig. 7 are given in Table 3. The grid convergence index (GCI), based on the generalised theory of the Richardson Extrapolation[52], is used to determine the relative error between the grids used. The index is generally considered to be the standard method for reporting grid uncertainty in numerical simulations involving CFD[53,54]. In this technique, the variable of interest for finer and coarser grids is used to estimate the relative error between them[52]. In Table 3, GCI_s and GCI_r are the relative errors obtained for the separation and reattachment locations respectively. It is seen that the relative errors reduces with increased grid refinement. The relative errors between Grid-5 and Grid-6, show that, for separation, the error is in the order of E-03 and for reattachment, it is in the order of E-04, both of which are quite small. Therefore, based on the heat flux and skin friction sensitivities, it would appear that the solution should be grid independent with Grid-5, so that further computations including $\theta_w = 18°$ and 16° are done with Grid-5.

https://doi.org/10.1017/S0001924000007740 Published online by Cambridge University Press



(a) Stanton number distributions (b) Pressure distributions

Figure 8. Stanton number and pressure distributions for $\theta_w = 24^\circ$ for condition B compared with experimental results; Note Olejniczak and Candle[16] represent reacting gas data.

4.0 RESULTS AND DISCUSSION

4.1 High enthalpy condition B

In this section the computational results are presented for the flow of air with a specific total enthalpy of 19MJ/kg designated as condition B[17,20]. Three ramp angles (θ_w) of 24°, 18° and 16° are investigated which correspond to fully separated (θ_w = 24° and 18°) and incipiently separated (θ_w = 16°) flows respectively. For all these ramp angles, both perfect and reacting gas (high temperature effects) data are presented. The reason for comparing with experimental data was because Mallinson[17,20] found that for the experimental data he obtained, the high temperature effects were negligible. A further comparison is made between the present results and those from Olejniczak and Candler[16], who compared their steady state computational results with Mallinson *et al*[17] experiments. The Olejniczak and Candler[16] data have been taken here from digitising the data from the literature, so that some inaccuracies may be present.

The comparison between the present and Olejniczak and Candler[16] data also complements as a code verification. As Roache[55] and Harvey *et al*[56] point out, comparing the solutions from two different computational codes can be a method of code verification. Although, the code verification process is typically restricted to the code developer, it is desirable to verify it for a new problem of interest[52].

$\theta_w = 24^\circ$

In Fig. 8(a), the Stanton number (S_t) distributions are compared with the experiments and the computational data of Olejniczak and Candler[16]. Olejniczak and Candler[16] carried out two-dimensional CFD simulations using Park's[26] two-temperature model including chemical reactions for the same geometric configuration and flow conditions as presently considered. The data of Olejniczak and Candler[16] taken here for comparison was obtained on their finest grid comprising of $1{,}024i \times 1{,}024j$.

As can be seen from Fig. 8(a) the distributions of heat flux over the initial length of the flat plate is a result of attached boundary layer growth. In this region, not much difference can be

https://doi.org/10.1017/S0001924000007740 Published online by Cambridge University Press

seen between the present perfect and reacting gas data, although the reacting gas data predicts less than perfect gas as expected. Nevertheless, both data sets slightly over predict the experimental data. The results of Olejniczak and Candler[16], on the other hand, closely match the experimental values. After $s/L_c \approx 0{\cdot}625$, where the heat flux reduction is seen, indicates separation. The precise location of separation will be shown later through through skin friction distributions.

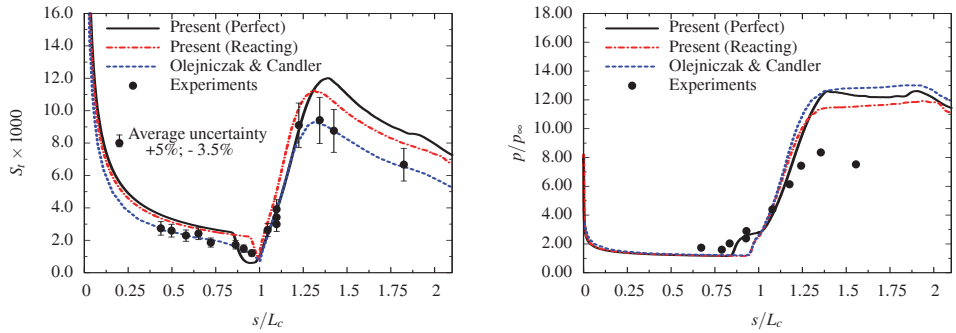
There are a number of differences that can be seen after $s/L_c \approx 0{\cdot}625$. The perfect gas data seem to over predict the separation size, while the reacting gas prediction appears to be closer to experimental values. This is also in close agreement with Olejniczak and Candler[16] data. Within the recirculation region upstream of the corner, all the computational data compare well with experiments, although the scale of recirculation region is smaller in reacting gas. Such a feature is also noted by Matsumoto *et al*[19] for a chemically reactive air flow over a two-dimensional compression corner.

Downstream from the corner after the separated shear layer has reattached to the plate, some interesting trends are seen. As the neck region forms, the thickness of the shear layer is reduced increasing the heat flux to a peak value due to steeping of temperature gradients. Close to the vicinity of this peak, reattachment occurs. The location of reattachment based on skin friction will be presented later. This is quite clearly seen in both CFD data and the experiments. However, some significant differences are noted. Firstly, none of the CFD data matches the experimental peak heat flux location which is at $s/L_c \approx 1{\cdot}37$. They all seem to under predict the peak heat flux by a considerable margin. Nevertheless, the present CFD reacting gas results seem closest to most of the experimental points over the ramp surface apart from the maximum heat flux location. In contrast, the data of Olejniczak and Candler[16] severely under predicts, except in the immediate vicinity of the corner location. Suffice to say at this stage that the present solution with Grid-5 ($570i \times 102j$) and reacting gas assumption seem to predict results closer to the experimental data on the ramp. It should be noted that the average uncertainty in experiments is around +9% and –6·5% and is generally higher in downstream region post reattachment.

The under prediction of the peak heat flux with respect to experiments suggests that a transition in the separated shear layer might have occurred or that the experimental data is affected by three-dimensional effects. Rudy *et al*[8] numerically found that for the experiments of Holden and Moselle[6] for fully separated flows, three-dimensional simulation showed better agreement with experimental data. In contrast, Lee and Lewis[9] found good agreement for the same experimental data of Holden and Moselle[6] with two-dimensional assumption. These comparisons would indicate that while possibly the flow may not be entirely two-dimensional, the experiments indicate that it may be so at least in the mid span region[17]. Nevertheless, transition downstream of reattachment is still a possibility. The current CFD and Olejniczak and Candler[16] data, of course, are purely laminar and two-dimensional. Downstream of reattachment the shear layer grows and the flow becomes parallel to the surface showing a decrease in heat flux.

Figure 8(b) shows the normalised pressure distribution in comparison with experiments and also Olejniczak and Candler[16] data. On the flat plate upstream of the corner, the CFD results from the three sets are in close agreement and indicate a typical distribution of pressure due to the boundary layer growth. It should be noted that there are no experimental data to compare in this upstream region. A pressure increase and plateau can be seen to occur which is a consequence of adverse pressure gradient which leads to separation. Based on the location of inflection in surface pressure and decrease in heat flux from the reacting gas model, the separation location may be considered to occur at $s/L_c \approx 0{\cdot}75$. This is in close agreement with Olejniczak and Candler[16] data.

https://doi.org/10.1017/S0001924000007740 Published online by Cambridge University Press



(a) Stanton number distributions (b) Pressure distributions

Figure 9. Stanton number and pressure distributions for $\theta_w = 18^\circ$ for condition B compared with experimental results; Note Olejniczak and Candler[16] represent reacting gas data.

The pressure inflection in perfect gas prediction occurs slightly ahead of that of the reacting gas prediction. A similar trend was also noted with the heat flux over this region. This again shows that the scale of separated region is over predicted with the perfect gas model. The CFD data of Olejniczak and Candler[16] almost matches the present CFD reacting gas data in the separated region and the two sets of data also compare quite well with experiments. Further, the plateau pressure in the separated region upstream of the corner is nearly the same for both perfect and reacting gas data.

Downstream from the corner, the CFD results from all the three sets more or less equally over predict the peak experimental values. However, some agreement with experiments is seen immediately downstream of the corner with present CFD results. The Olejniczak and Candler[16] data on the other hand show larger deviation from the experiments. The location of the peak pressure indicating the shear layer reattachment to the plate matches the peak heat flux location. Beyond this, the present reacting gas computation shows a much reduced pressure in comparison to both perfect gas and Olejniczak and Candler[16]data, but no where close to the experiments. It is possible that with chemical reactions occurring, the recompression shock angle changes and thereby alter the pressure rise. As will be shown later, the chemical reactions are dominant in the neck region and downstream of it. On the other hand, lower pressures in the experiments may, indicate transition or three-dimensional effects as noted earlier. Downstream of the peak, the oscillations seen are due to the expansion waves generated as a result of shock/shock interaction on the ramp reflect between the ramp surface and the recompression shock. Consequently, pressure decreases due to expansion and increases due to recompression, which is evident from the pressure distribution downstream of reattachment.

$\theta_w = 18^\circ$

In Fig. 9(a), Stanton number distributions obtained through the present computations are compared with those of Olejniczak and Candler[16] and the experiments. Similar to ramp angle of $\theta_w = 24^\circ$, the simulation at this angle is carried out under the two-dimensional assumption and so was the data of Olejniczak and Candler[16]. The data of Olejniczak and Candler[16] correspond to a grid size of $512i \times 512j$.

Upstream of the corner, similar to $\theta_w = 24^\circ$, not much difference between the two gas models is evident. The data, however, over predict the experimental values. Olejniczak and Candler[16] data seem to be in good agreement with experiments in this region. By $s/L_c \approx 0{\cdot}875$ heat flux

https://doi.org/10.1017/S0001924000007740 Published online by Cambridge University Press

reduces, indicating flow separation. Interesting differences can be noted here. Primarily, the separated region as estimated by the perfect gas is relatively large while the reacting gas data predicts a very small separated region. The experimental data together with the present and Olejniczak and Candler[16] data indicate a classical V-shape distribution, typically indicating incipiently separated flow. For condition B, the incipient separation angle as determined experimentally by Mallinson[17] is 15 ± 1°, so that at $\theta_w = 18°$, the flow should have just past incipient separation. Also, from the experimental interferograms of this configuration a small separated region at the corner is evident[17]. There is therefore some uncertainty with both computations with regard to separation.

Downstream of the corner, as the separated shear layer reattaches to the plate, heat flux rises to its peak value. The characteristics of the distributions are quite similar to those for $\theta_w = 24°$. With respect to the quantitative comparison between the data sets, some significant differences are noted. The present results are in reasonable agreement immediately after the corner. Close to reattachment and downstream, they are considerably higher than those of experiments. Since the scale of the separated region is much smaller in a reacting gas, the peak heat flux location moves upstream of that of perfect gas and is close to the experimental peak location. The CFD data of Olejniczak and Candler[16] seem to agree with experiments better both upstream and downstream of the corner.

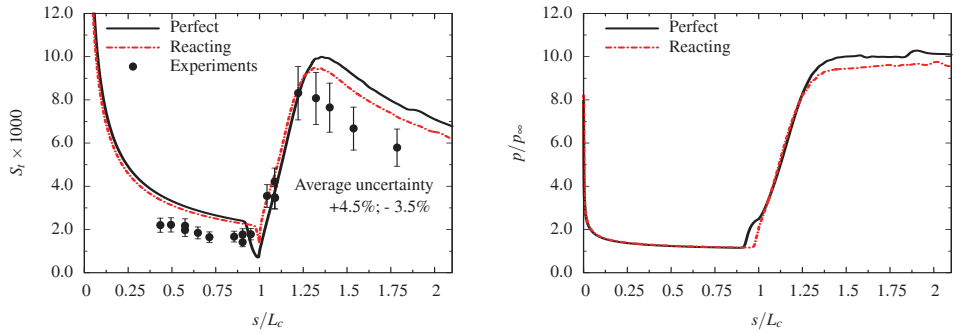
In Fig. 9(b), normalised pressure distributions are shown. Upstream of the corner over the flat plate, not much difference is noted between the two computations. In the vicinity of the corner, a pressure rise can be seen to occur at $s/L_c \approx 0{\cdot}87$ with the perfect gas, while for the reacting gas, the extent is rather small and occurs at $s/L_c \approx 0{\cdot}93$. The data of Olejniczak and Candler[16] is in close agreement with the present reacting gas data, suggesting a very small separated region is present. In comparison with experiments, both computations underestimate the scale of the separated region.

Immediately downstream of the corner, all three sets of computational data seem to be in fair agreement with the experimental data up to $s/L_c \approx 1{\cdot}2$ but beyond this they all over predict the experiments considerably as was noted with the case of $\theta_w = 24°$. The data of Olejniczak and Candler[16] shows much higher pressures than the present computations and also experiments. After reaching a peak the experimental data, shows a decrease in pressure while the CFD data all show a plateau up to $s/L_c \approx 1{\cdot}875$ before showing a decrease far downstream. While the experimental data points are not many on the ramp surface to make any definitive prediction, there is no indication of any plateau unlike the CFD data. All that can be said, therefore, is that while the perfect gas prediction indicates a clearly separated region as in the experiments, the reacting gas calculations indicate the possibility of a very small separated region. The agreement, post reattachment is very poor with experiments with all the CFD calculations.

$\theta_w = 16°$

Figure 10(a) presents the Stanton number distributions over a $\theta_w = 16°$ ramp compared with experiments. The data from Olejniczak and Candler[16] is not available for this configuration and hence it could not be used for comparison here. Upstream of the corner, as for the previous angles, both the CFD calculations over predict the experimental values considerably. As the corner is approached, the classical V-shape distribution is seen for the reacting gas data, suggesting that the flow is incipiently separated for $\theta_w = 16°$. The perfect gas data seem to indicate a very small separated region but over predicts both the experiments and the reacting gas data. From the experimental data, it is not clear whether the heat flux distribution is V-shaped (sharp) or slightly rounded (Mallinson[17]) but more likely to be incipiently separated.

https://doi.org/10.1017/S0001924000007740 Published online by Cambridge University Press



(a) Stanton number distributions (b) Pressure distributions

Figure 10. Stanton number and pressure distributions for $\theta_w = 16^\circ$ for condition B compared with experimental results.

Downstream from the corner, the heat flux rises to its peak and then falls downstream on the ramp surface. As can be seen from the figure, the CFD data of reacting gas past the corner for $s/L_c \leq 1{\cdot}25$ is in close agreement with experiments, after which both the CFD data considerably over predict the heat flux the perfect gas more so. The peak locations of both CFD data are downstream from that of experimental peak. The peak in the reacting gas, however, seems to be nearer to the experiments. This is possibly because both the reacting gas data and experiments seem to indicate incipient separation while the perfect gas predicts a slightly larger separated region.

The normalised pressure distributions are shown in Fig. 10(b). The computational data could not be compared with experiments, since the pressure measurements were not provided for this configuration in Mallinson[20]. Up stream of the corner, no difference between the two sets of CFD data are evident. Close to the corner ($s/L_c \approx 0{\cdot}875$), a pressure rise and inflection is seen in the perfect gas data, which corresponds to the same location where the rounded distribution in heat flux begins to occur, indicating the presence of a small separation bubble. On the other hand, no such indication is evident in reacting gas data which again is consistent with the heat flux distribution, thereby suggesting incipient separation condition.

Downstream from the corner the pressure plateaus after reaching a peak similar to those for the corner angle of 18°. Up to the peak, not much of a difference is seen between the two models. Further down, the pressure in the reacting gas is lower than that of the perfect gas.

4.2 Skin friction distributions

In his experiments, Mallinson[17,20] measured only the surface heat flux and pressures. Similarly, the CFD data by Olejniczak and Candler[16] also dealt with only heat flux and pressures. However, in addition to the above two properties, skin friction also is an important property that characterises the separation and reattachment at a compression corner. To highlight this aspect of the interaction flow, in this section, we discuss skin friction distributions for the compression corner flows considered earlier.

In Fig. 11, the skin friction distributions are shown for both perfect and reacting gas for $\theta_w = 24^\circ$. The skin friction passes from positive to negative indicating separation and in the reverse manner at reattachment. Most notable is the reduction of separation bubble in the reacting gas model. Separation occurs at $s/L_c \approx 0{\cdot}649$ in the perfect gas, where as in the reacting gas it occurs

https://doi.org/10.1017/S0001924000007740 Published online by Cambridge University Press

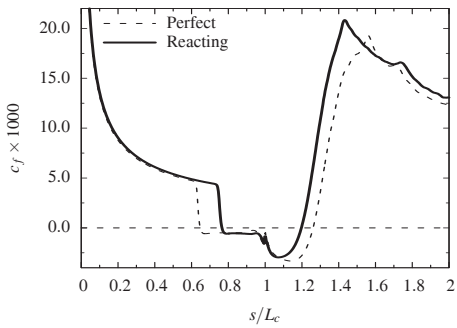


Figure 11. Skin friction distributions for $\theta_w = 24°$ for condition B.

at $s/L_c \approx 0{\cdot}767$. Similarly differences are noted at reattachment. Table 4 presents normalised distances for both the separation and reattachment.

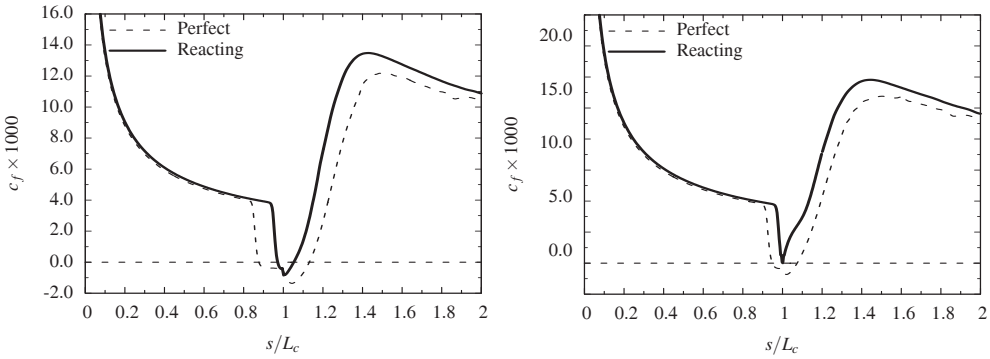
Downstream from the shear layer reattachment the skin friction rises sharply and reaches a peak similar to that of heat flux as a result of the thinning of the shear layer as the neck region is formed. The peak locations for reacting and perfect gas are at $s/L_c \approx 1{\cdot}43$ and $s/L_c \approx 1{\cdot}56$ respectively. The reacting gas peak location is consistent with both heat flux and pressure. Another feature to be noted is that the peak skin friction is higher with the reacting gas. Beyond the peak, the skin friction gradually reduces as the shear layer develops downstream.

In Fig. 11, between the location of separation and the corner ($s/L_c \approx 1$), the distribution of skin friction shows a plateau region and immediately after the corner it further increases in the negative direction with a rounded distribution before again passing through zero at reattachment. Firstly, the negative distribution seen upstream of the corner is due to recirculation bubble that has a clock wise direction. Past the corner, the increase in skin friction occurs due to the increased velocity gradients that develop within the recirculation bubble near reattachment. This is illustrated later through streamlines patterns at the corner. Such a feature in skin friction distribution is also evident from various numerical studies over compression corners. For example in the numerical work of Hung and MacCormack[3] and Marini[51], the skin friction distribution is presented for a ramp angle $\theta_w = 15°$ and 24° to compare with the experiments of Holden and Moselle [6] and Holden[57]. It is seen therein that both computations and experiments predict a higher skin friction downstream of the corner within the separation bubble for well separated flows, such as the present. However, these authors do not offer any explanation for such a feature.

Of further note is the magnitudes of skin friction variation that is apparent between perfect and reacting gas within the separation bubble. Upstream of the corner for the $\theta_w = 24°$, the skin friction values are nearly same in the reacting gas to those of perfect gas. However, downstream from the corner the reacting gas values are much lower, including the negative peak seen between $1 \le s/L_c \le 1{\cdot}2$. This feature is also noted by Furumoto *et al*[15] in a shock induced separation at high enthalpy condition.

In Fig. 11, very close to the corner a small oscillatory behaviour in skin friction is noted. This appears to occur with grid refinement, as shown in Fig. 6 of Section 3.2. Such a feature is also seen in heat flux, but on a much smaller scale. Although no physical explanation can be attributed to this at present, it would appear to be an artefact of the CFD scheme. This feature is seen in many computational results over compression corner and double cone geometries with refined grids (see for example Refs 19, 58, 59). Again, none of the authors offer any satisfactory explanation for this.

https://doi.org/10.1017/S0001924000007740 Published online by Cambridge University Press



(a) $\theta_w = 18°$ (b) $\theta_w = 16°$

Figure 12. Skin friction distributions for $\theta_w = 18°$ and $16°$ for condition B.

Table 4
Normalised separation and reattachment distances for different angles for flow condition B

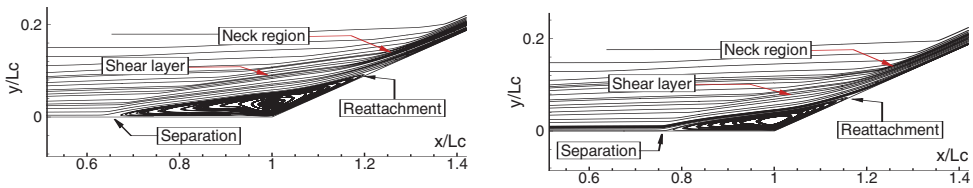
Angle θ_w	Model -	Separation s/L_c	Reattachment s/L_c
24°	Perfect gas	0·649	1·261
	Reacting gas	0·767	1·198
18°	Perfect gas	0·878	1·128
	Reacting gas	0·972	1·052
16°	Perfect gas	0·950	1·070
	Reacting gas	incipient separation	–

The skin friction disributions for $\theta_w = 18°$ and $\theta_w = 16°$ are shown in Fig. 12. As can be seen from these figures, the effects of reacting gas on the separation and reattachment are quite significant. With $\theta_w = 18°$, Fig.12(a), the distribution in skin friction indicates a small separation bubble. We also note that subsequent to reattachment the peaks of both reacting and perfect gas are nearly rounded rather than sharp as in the case of 24° angle ramp. Once again, the perfect gas results show a larger separated region.

The distributions of skin friction in Fig. 12(b) for $\theta_w = 16°$ is typical of incipient separation, especially with reacting gas. The perfect gas results give an indication of a small separation bubble. Overall, these results indicate that for this angle and at this flow condition, the flow is very nearly if not quite, incipiently separated and hence reinforces the conclusion of Mallinson[17,20] that the incipient separation angle is 16° ± 1°. These results also show typical characteristics of laminar two-dimensional viscous interaction with incipient separation[57].

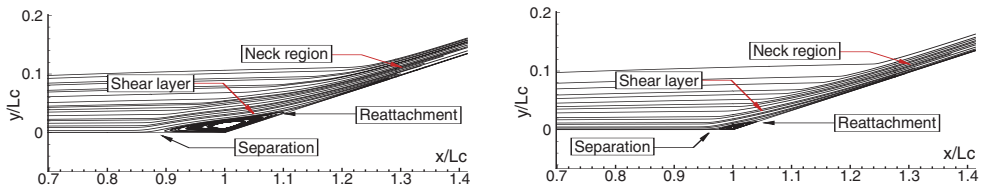
Table 4 shows separation and reattachment distances for reacting and perfect gas for the various angles.

https://doi.org/10.1017/S0001924000007740 Published online by Cambridge University Press



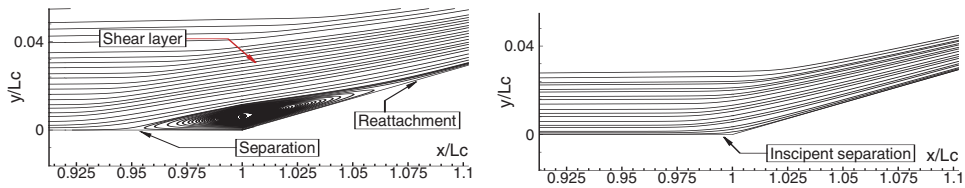
(a) Perfect gas (b) Reacting gas

Figure 13. Computed streamlines over the $\theta_w = 24^\circ$ compression corner.



(a) Perfect gas (b) Reacting gas

Figure 14. Computed streamlines over the $\theta_w = 18^\circ$ compression corner.



(a) Perfect gas (b) Reacting gas

Figure 15. Computed streamlines over the $\theta_w = 16^\circ$ compression corner.

4.3 Streamline patterns

Streamlines emphasising the separation/reattachment regions are shown in Figs 13, 14 and 15 for the three ramp angles with both perfect and reacting gas models. As previously discussed, the scale of the separated region can be seen to reduce with chemical reactions. Considering the streamlines for $\theta_w = 24^\circ$ in Fig. 13, we note that the formation of the neck region is more prominent with the reacting gas compared to the perfect gas. Consequently, the higher shear gradients with the reacting gas results in higher skin friction. This is reflected in skin friction being higher all through reattachment and beyond. The same features are present for $\theta_w = 18^\circ$ but on a smaller scale as seen from Fig. 14. In Fig. 15, a small separated region as predicted by perfect gas is seen, while in the reacting gas case (Fig. 15(b)) no clear separation is evident. All these features are consistent with the skin friction data discussed earlier.

4.4 Chemical reactions in the interaction region

The extent of chemical reactions is shown in Fig. 16 in regions of separation, reattachment and downstream for $\theta_w = 24^\circ$. As can be seen, N_2 decreases only marginally in the neck region and is consistent with the formation of N, although very low. It is also interesting to note that some degree of dissociation seems to occur behind the recompression shock, further towards the

https://doi.org/10.1017/S0001924000007740 Published online by Cambridge University Press

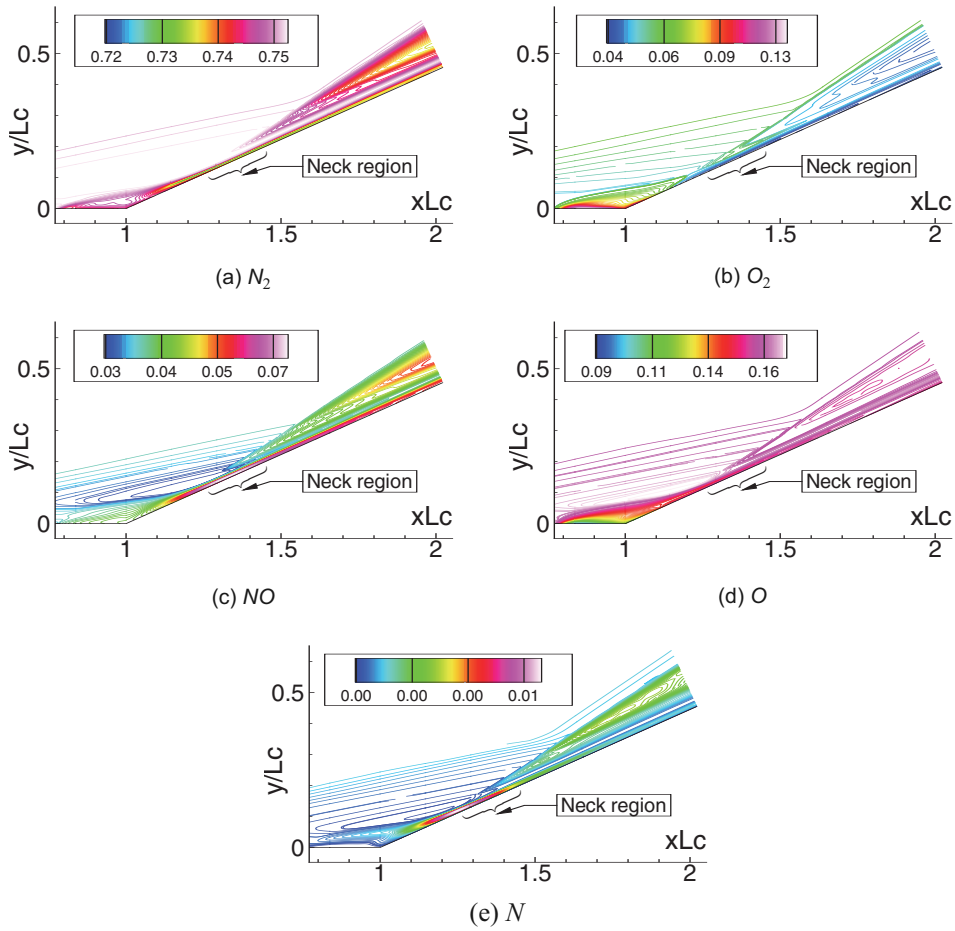


Figure 16. Contour map of species mass fractions for $\theta_w = 24°$ for condition B.

trailing edge. Considering Fig. 16(b), O_2 also dissociates in the neck region where the temperature is at its peak, and similar to N_2, dissociation of O_2 also occurs behind the recompression shock and within the shear layer downstream of reattachment. Some recombination is also seen within the separation bubble. This is also consistent with the reduction of O in the same region. This possibly might increase the heat flux marginally but the residence times of the recirculating flow are quite small (≈ 280-300μs) to have any appreciable effect on heat flux. Hence the concentration of O_2 is quite less. Formation of NO, as can be seen, is highest in the neck region and downstream of reattachment and behind the recompression shock. Some NO is also seen to form in the separated region, while other species are nearly frozen.

In a time-accurate numerical investigation of shock wave boundary layer interactions at nearly 18MJ/kg enthalpy for air, Furumoto *et al*[15], using a wedge/flat plate interaction found a reduction in the size of separation bubble ahead of the shock impingement location. This was attributed to the dissociative endothermic reactions occurring mainly post reattachment and as a consequence, reduction in pressures which led to a smaller separation.

https://doi.org/10.1017/S0001924000007740 Published online by Cambridge University Press

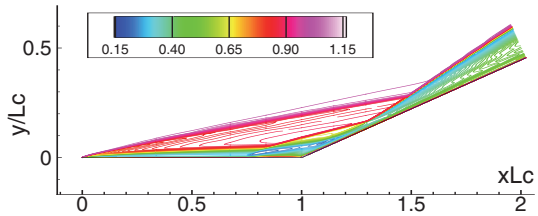
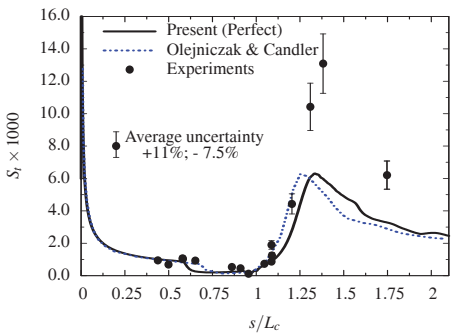
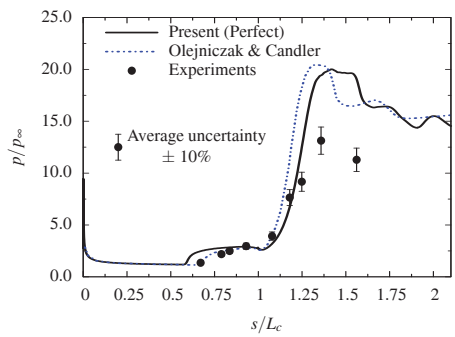


Figure 17. Contour map of ratio of vibrational-electronic to translational-rotational temperature (T_{v-e}/T_{v-r}) for $\theta_w = 24^\circ$ for condition B.



(a) Stanton number distributions



(b) Pressure distributions

Figure 18. Stanton number and pressure distributions for $\theta_w = 18^\circ$ for condition G compared with experimental results; Note Olejniczak and Candler[16] represent reacting gas data.

In Fig. 17, the ratio of vibrational-electronic to translational-rotational temperature (T_{v-e}/T_{v-r}) for condition B over the 24° ramp angle is shown, which indicates the degree of thermal nonequilibrium in the flow. As seen from the figure, the inviscid region is nearly in a thermal equilibrium. In the boundary layer upstream of the corner and in the shear layer downstream of reattachment, where peak temperature exists, the translational temperature is much higher than the vibrational temperature, even though the flow is thermally frozen. A further increase in translational temperature is evident across the reattachment shock and in the shear layer just upstream of the corner, where $T_{v-e}/T_{v-r} \approx 0{\cdot}2$. However, in the separation bubble upstream of the corner very close to the wall, a small region exists ($0{\cdot}8 \le s/L_c \le 1{\cdot}0$) where $T_{v-e}/T_{v-r} \approx 1$, suggesting that the flow there approaches thermal equilibrium.

The species concentration and the thermal nonequilibrium behaviour for ramp angles of 18° and 16° were very similar but on a much reduced scale.

4.5 Low enthalpy condition G

This section presents the results of specific total enthalpy of 2·8MJ/kg, designated as condition G in Mallinson[17,20]. Two ramp angles, 18° and 10° are considered and they correspond to fully

https://doi.org/10.1017/S0001924000007740 Published online by Cambridge University Press

separated and incipiently separated flows. Because of the low enthalpy nature of the flow, the simulated results are restricted to perfect gas assumption. This is also consistent with the experimental data of Mallinson[17,20]. However, for comparison purposes, the CFD data from Olejniczak and Candler[16] has been used to examine high temperature effects if any. As mentioned earlier, the Olejniczak and Candler[16] computation uses the Park's[26] scheme.

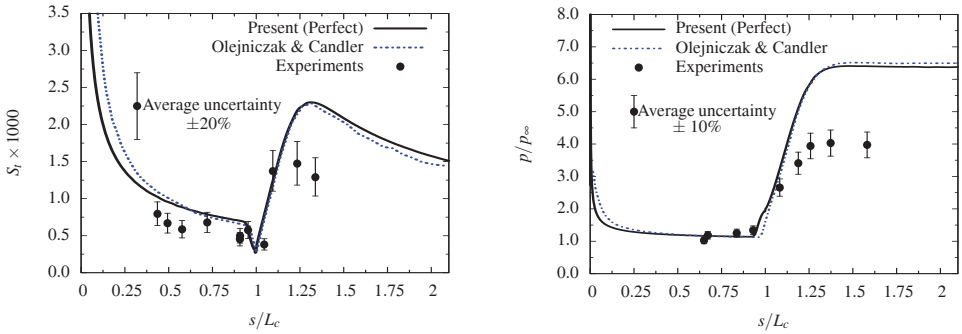
$\theta_w = 18°$

The Stanton number distributions compared with the experimental data and the data of Olejniczak and Candler[16] is presented in Fig. 18(a). The results from Olejniczak and Candler[16] were obtained on a $512i \times 512j$ grid, while the present data is obtained using Grid-5 ($570i \times 102j$). No difference is seen between the two computational predictions upstream of the corner at least up to $s/L_c \approx 0{\cdot}6$. Beyond this location, the heat flux decreases with a rounded distribution indicating a separated region. Just upstream of separation, both the CFD data seem to be in reasonable agreement with experiments. With regard to the separated region, the present data predict a slightly earlier separation than Olejniczak and Candler[16], while the two simulations are in reasonable agreement with each other and experimental data within the separated region. There is also reasonable agreement between the two CFD data and experiments in the vicinity of reattachment but the results diverge as the heat flux reaches peak values. The experiments indicate very high peaks along with large bands of uncertainty. Both the CFD results indicate peaks which are less by more than a factor of two compared with experiments. The situation is similar downstream of the peaks but here the experimental data is very sparse. The CFD data both show trends as expected.

Overall, the differences between experimental data and CFD are very large post reattachment. This gives rise to the suspicion that the flow in the experiments may have undergone a transition after reattachment. However, by examining the experimental heat transfer signals and the reasonable agreement of experimental data with the laminar perfect gas theory of Stollery and Bates[60], Mallinson[17,20] concluded that the flow remained laminar. In view of the larger Reynolds number of this flow condition, which is an order of magnitude higher than that of condition B, there is still a strong possibility that the flow may not be completely laminar after reattachment. However, the paucity of adequate experimental data downstream of the corner on the ramp renders this matter unresolved.

The pressure distribution is shown in Fig. 18(b) and compared with experiments and Olejniczak and Candler[16] data. As can be seen at $s/L_c \approx 0{\cdot}6$, an inflection in pressure followed by a plateau can be noted which indicates a well separated region. The pressure inflection and heat flux reduction locations are consistent with the beginning of separation. The exact location of separation would be identified later through skin friction distribution. Similar to heat flux, the pressure rise due to separation occurs upstream of that of Olejniczak and Candler[16] data thus over predicting the size of the separation bubble. The pressure distributions of Olejniczak and Candler[16] is in closer agreement with experiments within the separated region. The peak pressure in the current computation can be seen to occur slightly after that of Olejniczak and Candler[16] which is consistent with the larger scale of separated region predicted here. For both the CFD data, the heat flux peak and pressure peak locations do not quite correspond. Unlike the heat flux, the pressure in both the CFD data show an oscillatory behaviours which is due to recompression — expansion — recompression occurring on the ramp surface. These are caused as a result of reflection of the expansion fan originating from the slip stream at the shock/shock interaction and the surface. This behaviour, however, cannot be compared with experimental data as there is only one experimental data point downstream after the pressure peak.

https://doi.org/10.1017/S0001924000007740 Published online by Cambridge University Press



(a) Stanton number distributions (b) Pressure distributions

Figure 19. Stanton number and pressure distributions for $\theta_w = 10^\circ$ for condition G compared with experimental results; Note Olejniczak and Candler[16] represent reacting gas data.

$\theta_w = 10°$

The distributions of Stanton number along with the experimental data is shown in Fig. 19(a). The results from Olejniczak and Candler[16] correspond to the solution obtained on $512i \times 512j$ grid, while the current data is obtained on Grid-5 ($570i \times 102j$). As can be seen, difference between the two CFD data can be seen from far upstream but as the corner is approached, this difference diminishes and become indistinguishable in the vicinity of the corner. Both CFD data considerably differ from experiments ahead of the corner. After $s/L_c \approx 0{\cdot}875$, the heat flux reduces with a sharp v-shape distribution indicating an incipient separation. This will be confirmed further by skin friction distributions. A similar trend is also evident in the data of Olejniczak and Candler[16]. Both CFD data show fair agreement with the experiment in this region. Mallinson[17] found that experimentally the incipient separation angle was 10° ±2° while the theory predicted 9°.

Downstream from the corner as the heat flux rises, both the CFD data are in very close agreement and also match the experiments up to $s/L_c \approx 1{\cdot}125$. The two CFD data are in agreement with each other till the heat flux reaches peak, and diverge slightly thereafter. However, both data are much higher than the experiments. Once again, it should be pointed out that experimental data is very sparse on the ramp.

Figure 19(b) presents the pressure data. Upstream of the corner, both CFD results indicate similar values and are in good agreement with the experimental data. At $s/h \approx 0{\cdot}93$, an inflection in pressure can be identified in the present computation and is consistent with a very small separated/incipiently separated region and agrees well with the experimental data point. The Olejniczak and Candler[16] computations, however do not quite indicate separation, incipient or otherwise. Downstream from the corner as the pressure increases, there is a good agreement between the two CFD data and also with the experimental data at $s/L_c \approx 1{\cdot}12$. However as the pressure reaches it peak value, both CFD data over predict the experimental data. These large differences between CFD and experiments is similar to what is noted with heat flux. A constant pressure plateau that exists downstream of $s/L_c \approx 1{\cdot}12$ in both experiments and computations suggests that the shock/shock interaction is quite weak.

It may be noted that the plateau pressure ratio as determined by the two CFD calculations is quite close to the perfect gas inviscid value of $p/p_\infty = 6{\cdot}3$ while the experimental plateau

https://doi.org/10.1017/S0001924000007740 Published online by Cambridge University Press

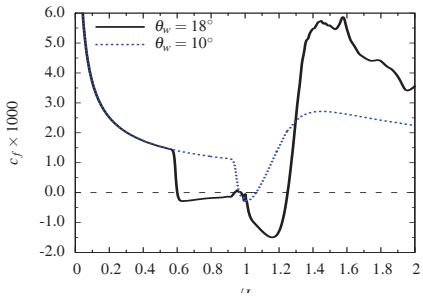


Figure 20. Skin friction distributions for $\theta_w = 18°$ and $10°$ for condition G.

Table 5
Normalised separation and reattachment distances for ramp angles 18° and 10° for flow condition G

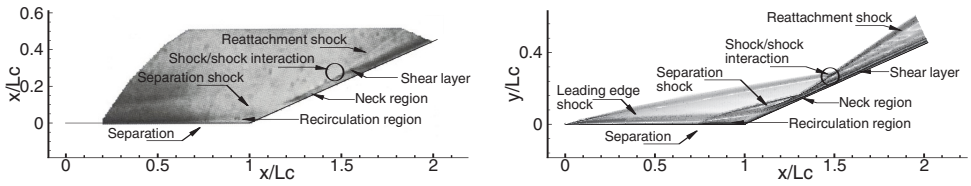
Ramp angle θ_w	Model -	Separation s/L_c	Reattachment s/L_c
$\theta_w = 18°$	Perfect gas	0·609	1·247
$\theta_w = 10°$	Perfect gas	0·968	1·064

indicates a value of about $p/p_\infty = 4{\cdot}0$ which is reduced by more than 60%. It is possible therefore that the flow past separation may have been influenced by three-dimensional effects from the boundary layer on the side skirts. Secondly, while the general uncertainty of pressure measurements is around ±10%, it may be higher under certain circumstances in low enthalpy flows such as condition *G*, where the signal to noise ratio of pressure traces on the ramp surface was generally lower.

In Fig. 20 skin friction distributions are shown for both $\theta_w = 18°$ and 10°. We note that, $\theta_w = 18°$ produces a well separated region with separation and reattachment at $s/L_c \approx 0{\cdot}609$ and $s/L_c \approx 1{\cdot}247$, respectively. Within the separated region, between $0{\cdot}9 \leq s/L_c \leq 1{\cdot}0$, skin friction seems to become positive before going negative again. This is indicative of a small secondary vortex circulating in the counter clock wise direction. This appears to be a characteristic of higher Reynolds number flow as it was not seen for the condition B. Very close to the corner, a small spike in skin friction can be seen, similar to what was also noted for flow condition B at $\theta_w = 24°$. As previously discussed, this is thought to be an artefact of computational modelling. After reattachment, skin friction rises sharply with the formation of neck region and then gradually decreases as the shear layer develops downstream. The oscillations seen after peak correspond oscillations due to multiple expansion and recompression.

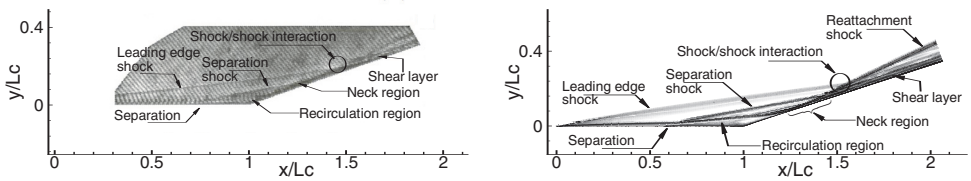
Considering the distribution for $\theta_w = 10°$, a small separated region can be identified with separation and reattachment at $s/L_c \approx 0{\cdot}968$ and $s/L_c \approx 1{\cdot}064$ respectively and this is consistent with the small pressure inflection noted in the pressure distributions. At $\theta_w = 10°$, therefore, the flow has just past incipient separation and is in accordance with the conclusions of Mallinson[17]. After reattachment, skin friction rises smoothly up to a maximum and then shows a gradual decrease downstream. Table 5 presents the summary of separation and reattachment distances for both $\theta_w = 18°$ and 10°.

https://doi.org/10.1017/S0001924000007740 Published online by Cambridge University Press



(a) Experimental infinite fringe[17] (b) Density gradient contours (Reacting gas)

Figure 21. Experimental and computational visualisation for $\theta_w = 24^\circ$ compression corner, Condition B (19MJ/kg).



(a) Experimental interferogram[17] (b) Density gradient contours (Perfect gas)

Figure 22. Experimental and computational visualisation for $\theta_w = 18^\circ$ compression corner, Condition G (2·8MJ/kg).

5.0 FLOW-FIELD COMPARISONS

Figure 21 shows the infinite fringe flow visualisation obtained from the experiments compared with the CFD data for well separated flows at conditions B. The flow features from the fringe diagram have been digitised from the photographic images so that some inaccuracies are possible. Here, the density gradient contours are shown to qualitatively compare the flow features. The density gradient contours are evaluated as $|\nabla\rho| = \sqrt{\rho_x^2 + \rho_y^2}$.

Considering flow condition B, Fig. 21, the boundary layer thickness predicted over the flat plate region matches the fringe pattern reasonably well. The location of separation and recirculation region in general are also in close agreement with the experimental fringe image. Other features that are in agreement are the separation shock, reattachment shock and the shear layer downstream. This indicates that the separation size and separation and reattachment locations are correctly modelled. In addition, the shock/shock interaction effect from the separation and the reattachment shocks is also correctly modelled and matches the experimental image.

In Fig. 22, low enthalpy condition G, the boundary layer thickness upstream of separation can be identified in both the images and agrees reasonably well. The location of separation can be seen to slight over predict in the CFD, while the separation shock is well captured which is also clearly visible in experimental image. Downstream from the corner, the interaction of separation and reattachment shock as modelled by the CFD, show some differences when compared with experiments. The location of the interaction occurs further downstream in the computation than what is seen in the experiment. Other features to note are the leading edge/recompression shock interaction which seem to match the experiments. Overall, the flow features are captured reasonably well.

https://doi.org/10.1017/S0001924000007740 Published online by Cambridge University Press

6.0 SUMMARY AND CONCLUSIONS

A computational investigation has been carried out for the flow over a compression corner for low and high enthalpy using a time-accurate solution and critically compared with that of a steady state solution and experimental data. Both incipient and fully separated flows have been investigated. Effects of high temperature-gas phenomena were considered for the high enthalpy case through modelling thermo-chemical nonequilibrium simulation in addition to finite rate chemistry. The comparisons show that CFD can reasonably predict the laminar SWBLI in the separated region at the corner. Nevertheless, some significant differences have been noted downstream on the ramp surface, particularly with regard to the location and magnitude of the peak heat flux and pressure and their subsequent distribution downstream. The study has shown that separation, reattachment and recirculation regions are affected by high temperature effects, in contrast to the conclusion drawn by Mallinson based on experimental data.

The investigation has shown that neither the time-accurate simulation presented here nor the steady state solution with the most refined grids as done by Olejniczak and Candler adequately describe all the aspects of shock wave/boundary layer interaction phenomena at high enthalpies that include high temperature effects. Both computational and experimental investigations are still needed to resolve all aspects of the problem.

ACKNOWLEDGEMENTS

The authors would like to express their sincere thanks to Dr Peter Jacobs of the University of Queensland for allowing us to use his Eilmer-3 solver. Thanks are also due to Dr Rowan Gollan of NASA Langley Research Center for his support in explaining various intricacies in these solvers and its usability.

REFERENCES

1. MACCORMACK, R.W. and PAULLAY, A.J. Computational efficiency achieved by time splitting of finite difference operators, 1972, 10th Aerospace Sciences Meeting, 17-19 January 1972, San Diego, CA, USA.
2. HUNG, C.M. and MACCORMACK, R.W. Numerical solutions of supersonic and hypersonic laminar flows over a two-dimensional compression corner, 1975, No 75-2, AIAA 13th Aerospace Sciences Meeting.
3. HUNG, C.M. and MACCORMACK, R.W. Numerical solutions of supersonic and hypersonic laminar compression corner flows, *AIAA J*, 1976, **14**, (4).
4. MACCORMACK, R.W. A numerical method for solving the equations of compressible viscous flow, *AIAA J*, 1982, **20**, (9), pp 1275–1281.
5. MADHAVAN, N.S. and SWAMINATHAN, V. Numerical solution of the supersonic laminar flow over a two dimensional corner using a implicit approach, *Int J Numerical Methods in Fluids*, 1986, **6**, pp 387-393.
6. HOLDEN, M.S. and MOSELLE, J.R. Theoretical and experimental studies of the shock wave-boundary layer interaction on compression surfaces in hypersonic flow, 1970, Technical Report ARL 70-0002, Aerospace Research Laboratories,Wright-Patterson AFB.
7. FAY, J.F. and SAMBAMURTHI, J. Laminar hypersonic flow over a compression corner using the hana code, 1992, AIAA-1992-2896, 27th AIAA Thermophysics Conference, 6-8 July 1992, Nashville, TN, USA
8. RUDY, D. H., THOMAS, J. L., KUMAR, A., GNOFFO, P. A. and CHAKRAVARTHY, S. R. Computation of laminar hypersonic compression-corner flows', *AIAA J*, 1991, **29**, (7), pp 1108–1113.
9. LEE, J.Y. and LEWIS, M.J. Numerical study of the flow establishment time in hypersonic shock tunnels', *J Spacecraft and Rockets*, 1993, **30**, (2), pp 152–163.

https://doi.org/10.1017/S0001924000007740 Published online by Cambridge University Press

10. GAITONDE, D.V. and SHANG, J.S. Accuracy of flux-split algorithms in high-speed viscous flows, *AIAA J*, 1993, **31**, (7), pp 1215–1221.
11. SIMEONIDES, G. AND HAASE, W. , Experimental and computational investigations of hypersonic flow about compression ramps, *J Fluid Mechanics*, 1995, **283**, pp 17–42.
12. GRUMET, A.A., ANDERSON, J.D. and LEWIS, M.J. A numerical study of shock wave/boundary layer interaction in nonequilibrium chemically reacting air: The effects of catalytic walls, 1991, AIAA-1991-0245, 29th Aerospace Science Meeting, 7-10 January 1991, Reno, NV, USA.
13. WU, S.T., ZHU, Y.H. and RITTER, A. A numerical study of the heat transfer due to shock-boundary layer interactions with finite-rate chemical reaction and radiation effects, 1994, AIAA-1994-0694, 32nd Aerospace Sciences Meeting & Exhibition, 10-13 January 1994, Reno, NV, USA.
14. GRASSO, F. and LEONE, G. Chemistry effects in shock wave boundary layer interaction problems, 1994, Proceedings of the IUTAM Symposium on Aerothermochemistry of Spacecraft and Associated Hypersonic Flows, 1994, Marseilles, France, pp 220–227.
15. FURUMOTO, G.H., ZHONG, X. and SKIBA, J.C. Numerical studies of real-gas effects on two-dimensional hypersonic shock-wave/boundary-layer interaction, *Physics of Fluids*, 1997, **9**, (1), pp 191–210.
16. OLEJNICZAK, J. AND CANDLER, G. V. , Computation of hypersonic shock interaction flow fields, 1998, Seventh AIAA/ASME Joint Thermophysics and Heat Transfer Conference, AIAA.
17. MALLINSON, S.G., GAI, S.L. and MUDFORD, N.R. The interaction of a shock wave with a laminar boundary layer at a compression corner in high-enthalpy flows including real gas effects, *J Fluid Mechanics*, 1997, **342**, pp 1–35.
18. DAVIS, J.-P. and STURTEVANT, B. Separation length in high-enthalpy shock/boundary-layer interaction', *Physics of Fluids*, 2000, **12**, (10), pp 2661-2687.
19. MATSUMOTO, A., ASO, S. AND KUROTAKI, T. A study on high temperature effects in shock wave/boundary layer interaction induced by compression corner, *Mem Fac Eng Kyushu University*, 2003, **63**, (2), pp 123–138.
20. Mallinson, S.G. Shock Wave/Boundary Layer Interaction at a Compression Corner in Hypervelocity Flows, 1994, PhD thesis, Aerospace & Mechanical Engineering, UNSW, Australian Defence Force Academy.
21. STALKER, R.J. and HORNUNG, H.G. The Australian National University free piston shock tunnel, 1971 T-3, Technical Report Laboratory Report PF-5, Physics Department, ANU, Canberra, Australia.
22. STALKER, R.J. Development of a hypervelocity wind tunnel, *Aeronaut J*, 1972, **76**, pp 374–384.
23. STALKER, R.J. Modern developments in hypersonic wind tunnels, *Aeronaut J*, 2006, **110**, (1103), pp 21–39.
24. JACOBS, P.A. and GOLLAN, R.J. The Eilmer3 code, 2010 Technical Report, Report 2008/07, Department of Mechanical Engineering, University of Queensland, Australia.
25. JACOBS, P.A., GOLLAN, R.J., DENMAN, A.F., O'FLAHERTY, B.T., POTTER, D.F., PETRIE-REPAR, P.J. and JOHNSTON, I.A. Eilmer's theory book: Basic models for gas dynamics and thermochemistry, 2010, Technical Report, Report 2010/09, Department of Mechanical Engineering, University of Queensland, Australia.
26. PARK, C. Review of chemical-kinetic problems of future NASA missions, I: Earth entries, *J Thermophysics and Heat Transfer*, 1993, **7**, (3), pp 385–398.
27. DEEPAK, N. R. , Computational Studies of Hypersonic High Enthalpy Separated Flows, 2010, PhD thesis, School of Engineering and Information Technology, University of New SouthWales, Australian Defence Force Academy.
28. VAN ALBADA, G.D., LEER, B.V. and ROBERTS, W.W. A comparative study of computational methods in cosmic gas dynamics, *Astronomy and Astrophysics*, 1982, **108**, (1), pp 76–84.
29. LEER, B.V. Towards the ultimate conservative difference scheme. V. A second-order sequel to Godunov's method, *J Computational Physics*, 1979, **32**, pp 101–136.
30. ANDERSON, W.K. and THOMAS, J.L. A comparison of finite volume flux vector splittings for the Euler equations, *AIAA*, 1986, **24**, (9), pp 1453–1460.
31. WADA, Y. and LIOU, M.S. A flux splitting scheme with high-resolution and robustness for discontinuities, 1994, AIAA-1994-83, 32nd Aerospace Sciences Meeting and Exhibition10-13 January 1994, Reno, NV, USA.
32. GOLLAN, R.J. The Computational Modelling of High-Temperature Gas Effects with Application to Hypersonic Flows, 2008, PhD thesis, Department of Mechanical Engineering, University of Queensland, Australia.

https://doi.org/10.1017/S0001924000007740 Published online by Cambridge University Press

33. AIT-ALI-YAHIA, D. A Finite Element Segregated Method for Thermo-Chemical Equilibrium and Nonequilibrium Hypersonic Flows Using Adapted Grids, 1996, PhD thesis, Concordia University.
34. MOTT, D.R. New Quasi-Steady-State and Partial-EquilibriumMethods for Integrating Chemically Reacting Systems, 1999, PhD thesis, The University of Michigan, USA.
35. GORDON, S. and MCBRIDE, B.J. Computer program for calculation of complex chemical equilibrium compositions and applications: I Analysis, 1994, Technical Report Reference Publication 1311, NASA.
36. MCBRIDE, B.J. and GORDON, S. Computer program for calculation of complex chemical equilibrium compositions and applications: II User manual and program description, 1996, Technical Report Reference Publication 1311, NASA.
37. GUPTA, R.N., YOS, J.M., THOMPSON, R.A. and LEE, K.-P. A review of reaction rates and thermodynamic and transport properties for an 11-species air model for chemical and thermal nonequilibrium calculations to 30,000K, 1990, Technical Report 1232, NASA.
38. PARK, G. Hypervelocity Aerothermodynamics of Blunt Bodies Including Real Gas Effects, 2010, PhD thesis, School of Engineering & IT, University of New South Wales, Australian Defence Force Academy.
39. POTTER, D.F. Modelling of radiating shock layers for atmospheric entry at Earth and Mars, 2010, PhD thesis, Department of Mechanical Engineering, University of Queensland, Australia.
40. NG, W.F., MITCHELL, C.R., AJMANI, K.A.C., TAYLOR, I. and BROCK, J.S. Viscous analysis of high speed flows using an upwind finite volume technique, 1989, AIAA-89-0001, 27th AIAA Aerospace SciencesMeeting, 9-12 January 1989, Reno, NV, USA.
41. RIZZETTA, D. and MACH, K. Comparative numerical study of hypersonic compression ramp flows, 1989, AIAA-89-1877, 20th AIAA Fluid Dynamics, Plasma Dynamics and Lasers Conference, 12-19 June 1989, Buffalo, NY, USA.
42. GNOFFO, P.A. CFD validation studies for hypersonic flow prediction, 2001, 2001-1025, 39th AIAA Aerospace Sciences Meeting & Exhibition, 8-11 January 2001, Reno, NV, USA.
43. DRUGUET, M.-C., BEN-DOR, G. and ZEITOUN, D. The interaction of supersonic and hypersonic flows with a double cone: comparison between inviscid, viscous, perfect and real gas model simulations, 2007, Vol 2, 26th International Symposium on ShockWaves, Gottingen, Germany.
44. DRUGUET, M.-C., CANDLER, G.V. and NOMPELIS, I. Effects of numerics on Navier-Stokes computations of hypersonic double-cone flows, *AIAA J*, 2005, **43**, (3), pp 616–623.
45. PARK, G., GAI, S.L. and NEELY, A.J. Aerothermodynamics behind a blunt boday at superorbital speeds, *AIAA J*, 2010, **48**, (8), pp 1804–1816.
46. JACKSON, A.P., HILLIER, R. and SOLTANI, S. Experimental and computational study of laminar cavity flows at hypersonic speeds, *J Fluid Mechanics*, 2001, **427**, pp 329–358.
47. PAPADOPOULOS, P., VENKATAPATHY, E., PRABHU, D. and LOOMIS, M.P. Current grid-generation strategies and future requirements in hypersonic vehicle design, analysis and testing, *Applied Mathematical Modelling*, 1999, **23**, (9), pp 705–735.
48. BERTIN, J.J. and CUMMINGS, R.M. Critical hypersonic aerothermodynamic phenomena, *Annual Review of Fluid Mechanics*, 2006, **38**, pp 129–157.
49. ICEM-CFD, 2008, ANSYS ICEM CFD, 2009, Ansys Inc, Southpointe, 275 Technology Drive Canonsburg, PA 15317, USA. URL: http://www.ansys.com/
50. CANDLER, G.V., NOMPELIS, I. and HOLDEN, M.S. Computational analysis of hypersonic laminar viscous inviscid interactions, 2000, AIAA-2000-0532, 38th AIAA Aerospace Sciences Meeting and Exhibition, 10-13 January 2000, Reno, NV, USA.
51. MARINI, M. Analysis of hypersonic compression ramp laminar flows under sharp leading edge conditions, *Aerospace Science and Technology*, 2001, **5**, (4), 257–271.
52. ROACHE, P.J. Quantification of uncertainty in computational fluid dynamics, *Annual Review of Fluid Mechanics*, 1997, **29**, pp 123–160.
53. AIAA 1994, Policy statement on numerical accuracy and experimental uncertainty', *AIAA J*, 32, (1), (3), (editorial).
54. ROACHE, P.J., GHIA, K.N. and WHITE, F.M. Editorial policy statement on the control of numerical accuracy, *ASME J Fluids Engineering*, 1986, **108**, (2).
55. ROACHE, P. J. Verification of codes and calculations, *AIAA J*, 1998, **36**, (5), pp 696–702.
56. HARVEY, J.K., HOLDEN, M.S. and WADHAMS, T.P. Code validation study of laminar shock/boundary layer and shock/shock interactions in hypersonic flow Part B: Comparison with Navier-Stokes and DSMC solutions, 2001, AIAA-2001-1031, 39th Aerospace Sciences Meeting and Exhibition, 8-11 January 2001, Reno, NV, USA.

https://doi.org/10.1017/S0001924000007740 Published online by Cambridge University Press

57. HOLDEN, M.S. A study of flow separation in regions of shock wave-boundary layer interaction in hypersonic flow, 1978, AIAA 78-1169, 11th AIAA Fluid and PlasmaDynamics Conference, 10-12 July 1978, Seattle, WA, USA.
58. CANDLER, G.V., NOMPELIS, I. and DRUGUET, M.-C. Navier-Stokes predictions of hypersonic double-cone and cylinder-flare flow fields, 2001, AIAA 2001-1024, 39th AIAA Aerospace Sciences Meeting & Exhibition, 8-11 January 2001, Reno, NV, USA.
59. NOMPELIS, I., CANDLER, G.V., MACLEAN, M., WADHAMS, T.P. and HOLDEN, M.S. Numerical investigation of double-cone flow experiments with high-enthalpy effects, 2010, AIAA 2010-1283, 48th AIAA Aerospace Sciences Meeting/New Horizons Forum and Aerospace Exposition, 4-7 January 2010, Orlando, FL, USA.
60. STOLLERY, J.L. and BATES, L. Turbulent hypersonic viscous interaction, *J Fluid Mechanics*, 1974, **63**, (1), pp 145–156.

https://doi.org/10.1017/S0001924000007740 Published online by Cambridge University Press